Enhancing Both Biodegradability and Efficacy of Semiconducting Polymer Nanoparticles for Photoacoustic Imaging and Photothermal Therapy

Yan Lyu,[†] Jianfeng Zeng,[‡] Yuyan Jiang,[†] Xu Zhen,[†] Ting Wang,[§] Shanshan Qiu,[‡] Xin Lou,[§] Mingyuan Gao,[‡] and Kanyi Pu*[†]*

[†]School of Chemical and Biomedical Engineering, Nanyang Technological University, Singapore, 637457

[‡]Center for Molecular Imaging and Nuclear Medicine, School for Radiological and Interdisciplinary Sciences (RAD-X), Soochow University, Collaborative Innovation Center of Radiation Medicine of Jiangsu Higher Education Institutions, Suzhou 215123, P. R. China

[§] Department of Radiology, The People's Liberation Army General Hospital, No. 28 Fuxing Road, Beijing 100853, China

ABSTRACT: Theranostic nanoagents are promising for precision medicine. However, biodegradable nanoagents with the ability for photoacoustic (PA) imaging guided photothermal therapy (PTT) are rare. We herein report the development of biodegradable semiconducting polymer nanoparticles (SPNs) with enhanced PA and PTT efficacy for cancer therapy. The design capitalizes on the enzymatically oxidizable nature of vinylene bonds in conjunction with the polymer chemistry to synthesize a biodegradable semiconducting polymer (DPPV) and transform it into water-soluble nanoparticles (SPNV). As compared with its counterpart SPN (SPNT), the presence of vinylene bonds within the polymer backbone also endows SPNV with the significantly enhanced mass absorption coefficient (1.3 fold) and photothermal conversion efficacy (2.4 fold). As such, SPNV provides the PA signals and the photothermal maximum temperature higher than SPNT, allowing to detect and photothermally ablate tumor in living mice in a more sensitive and effective way. Our study thus reveals the general molecular design to enhance the biodegradability of optically-active polymer nanoparticles meanwhile to dramatically elevate their imaging and therapeutic capabilities.

KEYWORDS: photoacoustic imaging, photothermal therapy, polymer nanoparticles, cancer therapy

Theranostic nanoagents that integrate real-time diagnosis with therapeutic capability can accurately target diseased tissues and optimally exert therapy,[1, 2] representing a way for cost-effective precision medicine.[3, 4] In comparison with radioactive,[5, 6] magnetic[7] and ultrasound[8, 9] imaging agents, optical nanoagents that only utilize light to generate diagnostic signals and trigger therapeutic process have attracted more attention for cancer therapy.[10-12] In particular, photothermal nanotheranostics not only can induce localized hyperthermia in tumor to directly eradicate cancer cells but also could potentially generate anti-tumor immunological effects.[13] Till now, most photothermal nanotheranostic systems rely on fluorescence as the signal readout, and thus share the drawbacks of shallow penetration and tissue autofluorescence, partially compromising imaging sensitivity.[14, 15] In contrast, photoacoustic (PA) nanoagents that detect ultrasound after light excitation overcome such limitations and thus offer deeper tissue penetration and higher spatial resolution to guide photothermal therapy (PTT).[16, 17] Different from fluorescent nanotheranostics that has two competing process (fluorescence *vs* nonradioactive decay), both PA signals and PTT effect are related to photothermal conversion, making PA/PTT nanotheranostics easier to design in principle.[18-21]

Many near-infrared (NIR) light absorbing nanaoagents including small molecule dyes,[22, 23] porphysomes,[24, 25] peptide-/protein-based nanomaterials,[26-29] metallic nanoparticles,[30, 31] carbon nanotubes,[32, 33] and two-dimensional materials (TDMs)[20, 34] have been used for PA imaging or PTT. Among many other issues in their translation research, biodegradability of these nanoagents is one of the most essential concerns.[35]

In fact, there are some inorganic nanoparticles have been designed to undergo stimuli-responsive degradation.[36-39] However, the metal ions released from degradation of inorganic nanoparticles could still be a threat to biological systems. Thus, development of organic nanoagents with biodegradability is highly desired for PA/PTT nanotheranostics.

Semiconducting polymer nanoparticles (SPNs) have emerged as a class of optical agents for molecular imaging[40] and phototherapy.[41-43] They are made of completely organic ingredients including semiconducting polymers/oligomers and amphiphilic polymers, and thus naturally bypass the toxicity issue induced by heavy metal ions.[44] Dependent on the molecular structures of SPs, SPNs have been diversified for NIR fluorescence,[21, 45, 46] chemiluminescence,[47, 48] photoacoustic[49, 50] and afterglow imaging[51] as well as photodynamic[52] and photothermal applications.[21, 53, 54] In particular, SPNs can convert photo energy into heat with the photothermal conversion efficacy higher than carbon nanotubes and gold nanorods.[54, 55] Despite their great potential in PA/PTT nanotheranostics, SPNs with high biodegradability have not been reported. Although biodegradable polymers such as polyesters and polyamides are available,[56] simple introduction of these hydrolyzable units (ester, carbonate, amide *et al.*) into the backbone of SPs will certainly hamper electron delocalization and thus compromise the optical properties of SPNs. Thereby, the design for biodegradable SPNs remains to be revealed.

We herein report the synthesis of a biodegradable SPN with enhanced PA and PTT efficiencies for cancer therapy. The molecular design involves the incorporation of

vinylene bond as a structural unit into the backbone of SP. Because we recently found that the vinylene bonds tend to undergo π^2- π^2 cycloaddition with oxidants followed by hydrolysis,[51] the SPNs can be gradually broken down into small fragments in the biological environment abundant of oxidative species. In addition, the presence of vinylene bonds not only facilitates chain packing but also increases the mass absorption coefficients, leading to enhanced photothermal conversion and thus amplified PA and PTT efficiencies. In the following, the synthesis of the SPNs is described first, followed by studies of their optical and photothermal properties. Then, the biodegradability of the SPNs is studied under the *in vivo* mimetic conditions. At last, the proof-of-concept application of these SPNs as PA/PTT nanotheranostic agents is demonstrated in xenograft tumor mouse model.

RESULTS AND DISCUSSION

The biodegradable SP, poly{2,2'-[(2,5-bis(2-hexyldecyl)-3,6-dioxo-2,3,5,6-tetrahydropyrrolo[3,4-*c*]pyrrole-1,4-diyl)dithiophene]-5,5'-diyl-*alt*-vinylene} (DPPV), was synthesized through palladium-catalyzed Stille polymerization between 3,6-bis(5-bromothiophen-2-yl)-2,5-bis(2-hexyldecyl)pyrrolo[3,4-*c*]pyrrole-1,4(2*H*,5*H*)-dione (monomers 1) and trans-1,2-bis(tributylstannyl)ethene (monomers 2) (Figure 1a). In comparison, its analog poly{2,2'-[(2,5-bis(2-hexyldecyl)-3,6-dioxo-2,3,5,6-tetrahydropyrrolo[3,4-*c*]pyrrole-1,4-diyl)dithiophene]-5,5'-diyl-*alt*-thiophen-2,5-diyl} (DPPT, Figure 1b) without vinylene bonds was also synthesized according to the previous report. DPPV and DPPT were respectively co-precipitated with a

biodegradable amphiphilic polymer, poly(ethylene glycol) methyl ether-*block*-poly(lactide-*co*-glycolide) (PLGA-PEG), to endow the nanoparticles with good water solubility without interfering their biodegradability (Figure 1c). The nanoparticle core was formed by the hydrophobic interaction between the PLGA segments and DPPV or DPPT, while the nanoparticle surface was covered by the PEG segments. The resulting nanoparticles (SPNV&SPNT) showed similar average hydrodynamic diameters of ~36 nm and spherical morphologies, as indicated by dynamic light scattering (DLS) and transmission electron microscope (TEM), respectively (Figures 1d, e). After storage in the dark at 4 °C, the sizes of SPNV and SPNT remained almost the same for the first 15 days and slightly reduced by ~8 nm on day 22 (Figure S1, Supporting Information), which should be attributed to the hydrolysis of PLGA-PEG in aqueous solution.[57] Nevertheless, the solutions of both SPNV and SPNT remained transparent and the sizes did not further change (Figure 1f, Figure S1 in the Supporting Information).

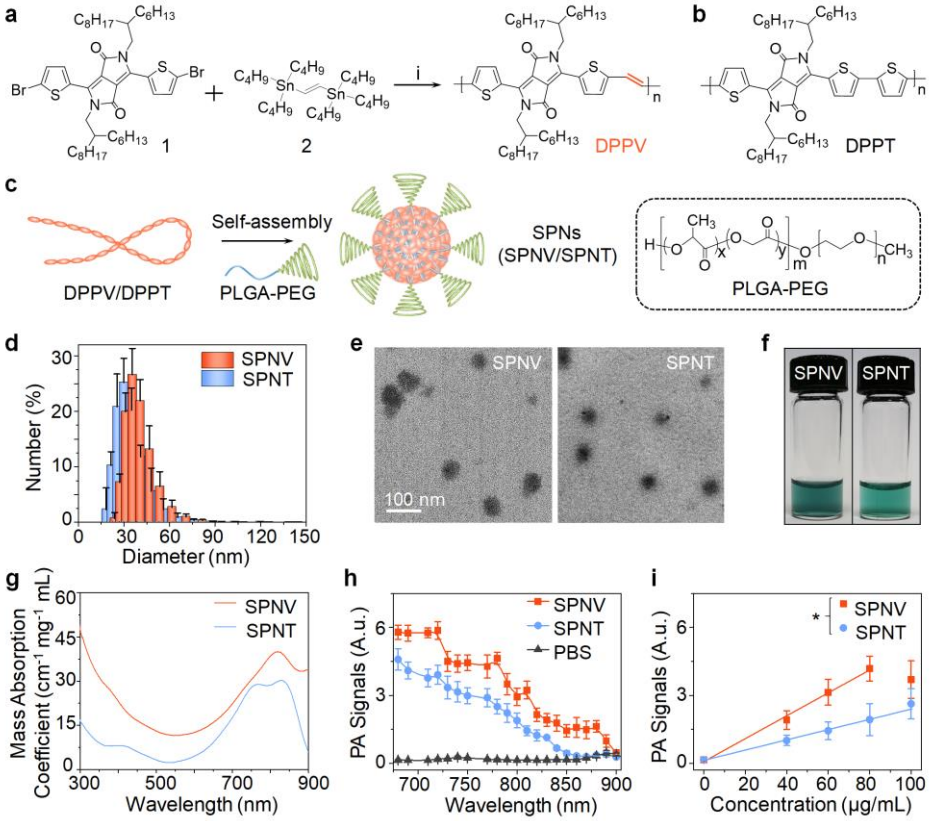

Figure 1. Synthesis and characterization of SPNs. (**a**) Synthetic route of DPPV. (i) $Pd_2(dba)_3$ and tri(*o*-tolyl)phosphine, toluene, 100 °C, 24 h. (**b**) Chemical structure of DPPT. (**c**) Chemical structure of PLGA-PEG and schematic illustration of the preparation of SPNs. DLS profiles (**d**), TEM images (**e**), photographs of the solutions (**f**) and absorption spectra (**g**) of SPNV and SPNT. (**h**) PA spectra of SPNV, SPNT and PBS. (**i**) PA intensities at 810 nm as a function of the concentrations of SPNV and SPNT from 0 to 100 μg mL^{-1} (R^2 = 0.992 and 0.995 for SPNV and SPNT respectively). The SPN solutions used in characterization were prepared in PBS buffer (pH 7.4). The solutions with the concentration of 60 μg mL^{-1} were used in photography and PA spectra measurements. A single laser pulse with energy of 100 mJ $pulse^{-1}$ (duration of 5 ns) and a pulse repetition rate of 10 Hz was used for PA intensity. Error bars were based on the standard deviations (SD) of three parallel samples. *Statistically significant difference in PA intensities for SPNV and SPNT with the concentration ranging from 0 to 80 μg mL^{-1} ($p < 0.01$, $n = 3$).

To study the effect of vinylene bonds on optical properties, the absorption and PA

spectra of SPNV and SPNT were measured and compared under physiological conditions. Both SPNs showed broad absorption in the NIR region ranging from 600 to 900 nm (Figure 1g), allowing NIR light to generate both PA and photothermal signals. Due to the presence of vinylene bonds, the absorption maximum of SPNV was located at 819 nm, which was similar to that of SPNT at 828 nm. Besides, because the repeat unit of DPPV had the lower molecular weight (803.31 g mol^{-1}) than DPPT (859.39 g mol^{-1}), the mass absorption coefficient of SPNV at 819 nm (40 cm^{-1} mg^{-1} mL) was 1.3-fold higher than that of SPNT (30 cm^{-1} mg^{-1} mL at λ=828 nm). Based on the molecular weight of the repeat unit, SPNV (32.1 cm^{-1} mol^{-1} mL) also showed 1.2-fold higher molar extinction coefficient than SPNT (25.8 cm^{-1} mol^{-1} mL). This was due to its more planar conformation in the presence of vinylene bonds that facilitated the electron delocalization.[58] The PA spectra of SPNs were acquired at the same concentration (60 μg mL^{-1}) by pulsed laser irradiation ranging from 680 to 900 nm (Figure 1h). Overall, the PA signals of SPNV were stronger than those of SPNT. Particularly, the PA signal of SPNV at 810 nm was 2.2-fold higher than that of SPNT. The good linear correlation between the PA signals and the concentrations of SPNs was observed for both SPNs (Figure 1i), indicating the feasibility for signal quantification. Note that the PA signal of SPNV was oversaturated above 80 μg mL^{-1}. These data confirmed that the presence of vinylene bonds in SPNV led to the higher mass absorption coefficient and stronger PA signals as compared to SPNT.

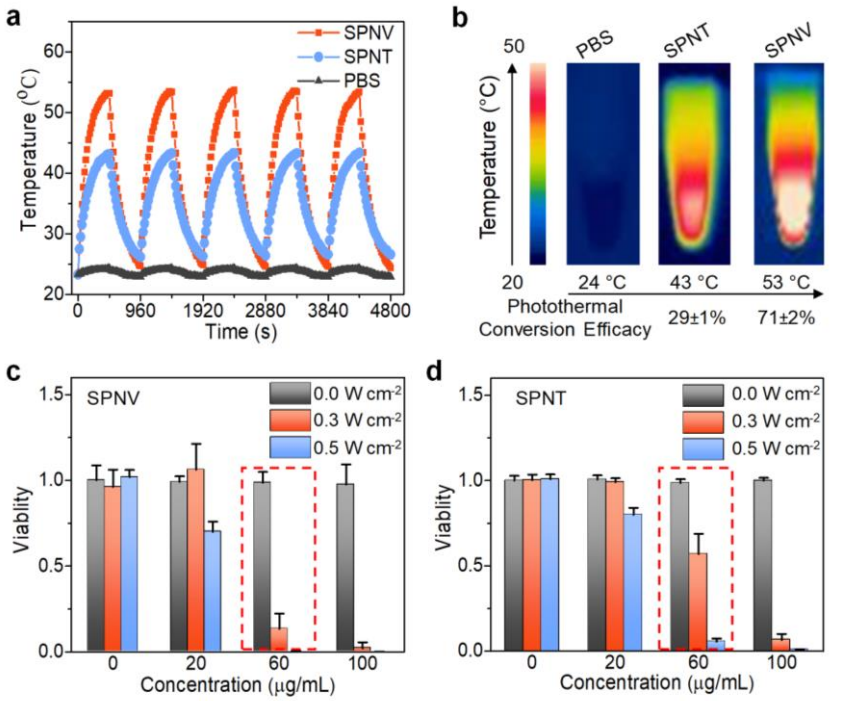

Figure 2. Photothermal characterization of SPNs and *in vitro* PTT cell experiments. (**a**) Photothermal heating and natural cooling cycles under the 808 nm laser irradiation with power density of 0.3 W cm^{-2}. [SPN]= 60 μg mL^{-1} in PBS buffer (pH 7.4). (**b**) Thermal images of SPNV, SPNT and PBS at their respective maximum temperatures. The maximum temperature values and photothermal conversion efficacies are indicated below the respective images. Relative viabilities of 4T1 cells after incubation with different concentrations (20, 60, 100 μg mL^{-1}) of SPNV (**c**) or SPNT (**d**) and irradiation under the 808 nm laser with different power densities (0.3, 0.5 W cm^{-2}) for 8 min. Error bars were based on the standard deviations (SD) of three parallel samples.

The photothermal properties of SPNV were studied and compared with SPNT at the same concentration under the NIR laser irradiation at 808 nm with the power density of 0.3 W cm^{-2}, which was lower than the maximum permissible exposure (MPE) for skin (0.33 W cm^{-2}). The temperatures of both SPN solutions gradually increased upon under laser irradiation and reached maximum at t=480 s (Figure 3a). However, the temperature of SPNV was higher than that of SPNT at each time point, while PBS

buffer just showed maximum temperature change by 1 °C because of the low power density applied. The maximum photothermal temperature of SPNV was 53 °C, 1.2-fold higher than that of SPNT (43 °C) (Figure 3b). The photothermal conversion efficacy of SPNV was calculated to be 71±2%, 2.4-fold higher than that of SPNT (29±1%) and also significantly higher than other inorganic photothermal agents such as gold nanorods, phosphorus quantum dots and TDMs.[20] The better photothermal performance of SPNV relative to SPNT should be ascribed to the presence of vinylene bonds within DPPV which resulted in more planar chain conformation and thus more compact chain packing within the nanoparticles.[59] Both SPNs had good photothermal stability as verified by the nearly unchanged maximum temperatures after 5 circles of heating and natural cooling (Figure 3a).

The PTT efficacies of both SPNs were firstly studied *in vitro*. 4T1 cells were incubated with different concentrations of SPNs for 3 hours before exposed to NIR laser. Then the cells were irradiated at 808 nm with the different power densities for 8 min and the cell viabilities were measured after incubation for another 12 h. With no laser irradiation, both SPNs did not affect the cell viabilities even at the concentration up to 150 μg mL^{-1}, indicating their good cytocompatibility (Figure S2, Supporting Information). Generally, for both SPNs, the cell viabilities decreased with increasing the nanoparticle concentrations or illumination power densities, while irradiation alone without SPN treatment had little effect on the cell viabilities (Figures 3c, d). However, SPNV was more effective in cell ablation than SPNT. When comparing at the concentration of 60 μg mL^{-1}, SPNV-mediated laser irradiation led to the cell viability

as low as 13%, which was 4.3-times lower than SPNT (57%). These data further confirmed SPNV was a better PTT agent than SPNT as a result of its higher photothermal conversion efficacy.

Biodegradability of both SPNs was studied under the solution conditions that mimic *in vivo* environment (Figure 2a). Myeloperoxidase (MPO), a peroxidase enzyme abundantly expressed in immune cells with the concentration as high as ~82.6 μg mL^{-1} in blood,[60] was chosen to study if SPNV and SPNT could be digested. In living animals, the reaction of MPO and hydrogen peroxide (H_2O_2) can generate strong oxidant, hypochlorous acid (HClO).[61] Upon incubation with MPO and H_2O_2, the absorption of SPNV gradually decreased (Figure 2b), while it remained the same without MPO (Figure 2c). After incubation for 48 h, the absorption peak of SPNV at 819 nm completely disappeared, indicating the full scission of π-conjugated backbone (Figure 2b). In contrast, SPNT could not be broken down by MPO as witnessed by the unchanged absorption (Figure 2c). These data demonstrated that the presence of vinylene bonds within DPPV made SPNV much easier to be degraded as compared to SPNT.

The biodegradability of SPNV was further verified in macrophage RAW264.7 cells. As the expression of MPO enzyme in RAW264.7 cells can be induced by stimulation with lipopolysaccharides (LPS), [62] the RAW264.7 cells were treated with LPS after incubation with SPNV. After stimulation with LPS for 30 hours, the cells were washed with PBS to remove the free SPNV nanoparticle and then harvested. The concentrations of SPNV inside cells were measured by absorption. The absorption maximum of SPNV

at 819 nm (276, 000 cells /mL) were 0.081, which was only 12% of that without LPS treatment (0.674) (Figure 2d). This further demonstrated the biodegradability of SPNV at cellular level.

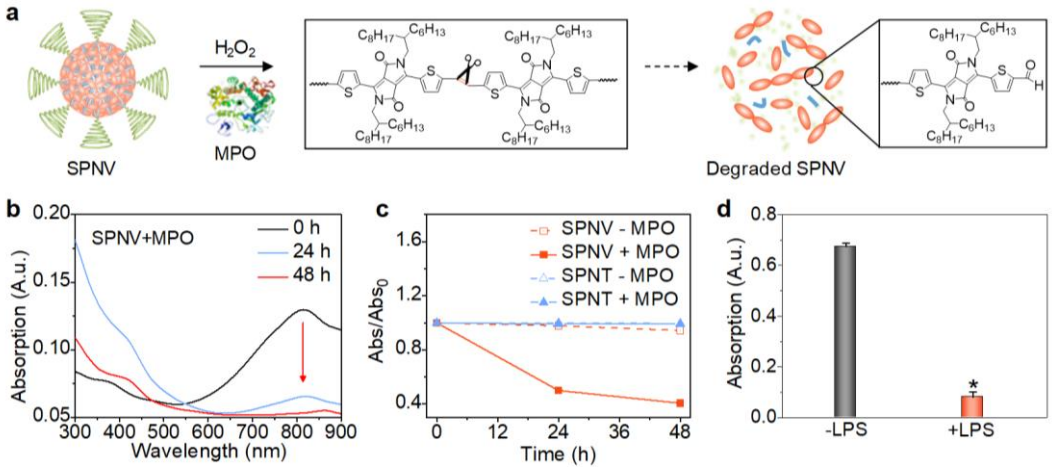

Figure 3. *In vitro* biodegradability study of SPNs. (**a**) Schematic illustration of the degradation of SPNV in the presence of MPO and H_2O_2. (**b**) Absorption spectra of SPNV in the presence of H_2O_2 (300 μM) and MPO (50 μg mL^{-1}) at 37 ºC for 0, 24, and 48 h in phosphate buffer (50 mM, pH = 7.0) containing NaCl (150 mM). (**c**) Absorption decrease (Abs/Abs_0) of SPNV at 819 nm and SPNT at 828 nm in the absence or presence of MPO (50 μg mL^{-1}) and H_2O_2 (300 μM) as a function of incubation time. [SPNs]= 3 μg mL^{-1}. (**d**) Absorption pf SPNV at 819 nm of 1 mL of the extracted solutions from 276, 000 macrophage RAW264.7 cells uptaking SPNV and treated with or without LPS. Error bars were based on the standard deviations (SD) of three parallel samples. *Statistically significant difference in cells treated with or without LPS ($p < 0.005$, $n = 3$).

The PA imaging capability of SPNV was studied and compared with SPNT in living

mice bearing xenograft 4T1 tumors. After systemic administration of SPNV or SPNT into the mice through tail vein, the PA images were longitudinally recorded and quantified under the excitation of pulse laser at 810 nm. The PA intensities gradually increased for both SPNs treated mice and reached its maxima at 6 h post-injection. At this time point, the PA intensity for SPNV-treated mice was 1.5-fold higher than that for SPNT-treated mice (Figures 4a, b). The real-time *in vivo* PA spectra extracted from the tumor regions for both SPNs showed the similar profiles to those in solutions (Figure 4c), confirming that the increased PA signals were generated from the nanoparticle accumulation. Because SPNV and SPNT had the same surface structure and size, their biodistribution were similar (Figure S3, Supporting Information). Thus, the stronger signals from the SPNV-treated mice relative to SPNT should result from the relatively higher PA brightness of SPNV.

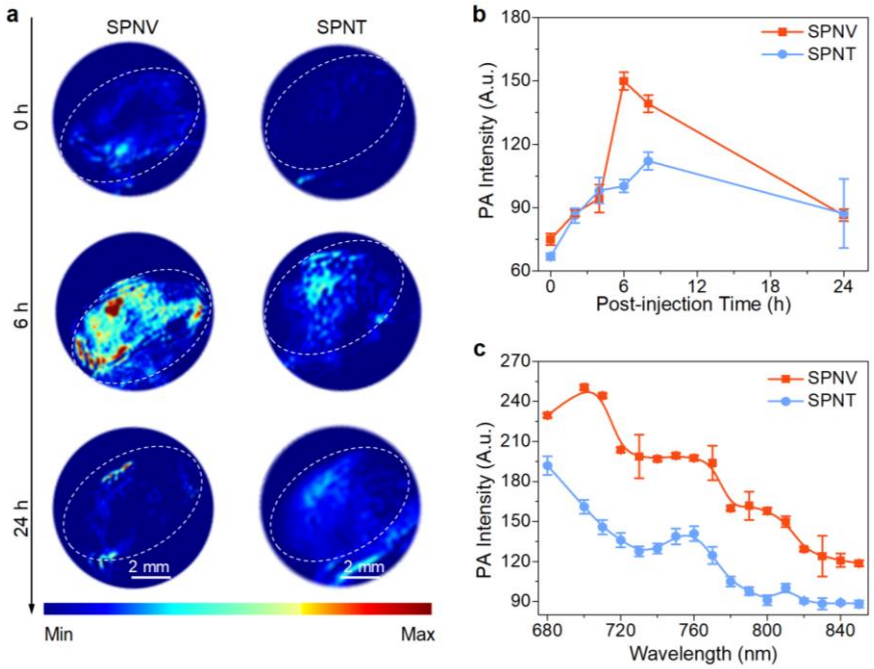

Figure 4. *In vivo* PA imaging of tumor in living mice. (**a**) PA images of living mice bearing xenograft 4T1 tumors at 0, 6 and 24 h after systemic administration of SPNV

or SPNT (6 mg kg^{-1} body weight). The PA images were acquired at 810 nm. The tumors are indicated with the white dashed circles. (**b**) Quantification of PA intensities of tumor regions as a function of post-injection time of SPNV or SPNT (n = 3). (**c**) Real-time *in vivo* PA spectra of tumors at the post-injection time of 6 h. Error bars were based on the standard deviations (SD) of three parallel samples.

The PTT capability of SPNV was tested and compared with SPNT. Because the PA signals reached maximum at 6 h post-injection of SPNs (Figure 4b), laser irradiation at 808 nm was conducted at this time point for 5 min with the power of 0.3 W cm^{-2}. The thermal images of mice and surface temperatures of tumors were recorded as a function of laser irradiation time (Figures 5a, b). The tumor temperatures gradually increased along with laser irradiation and reached plateau after irradiation for 4 min. At each time points, the maximum tumor temperatures of SPNV-treated mice were significantly higher than that of SPNT- or saline-treated mice. In particular, the maximum tumor temperature of SPNV-treated mice was 50 °C, 1.2-fold and 1.3-fold higher than that of SPNT- (42 °C) and saline-treated (39 °C) mice, respectively. Such a higher tumor temperature for SPNV-treated mice relative to SPNT-treated mice was consistent with the solution data, which was due to the higher photothermal conversion efficacy of SPNV.

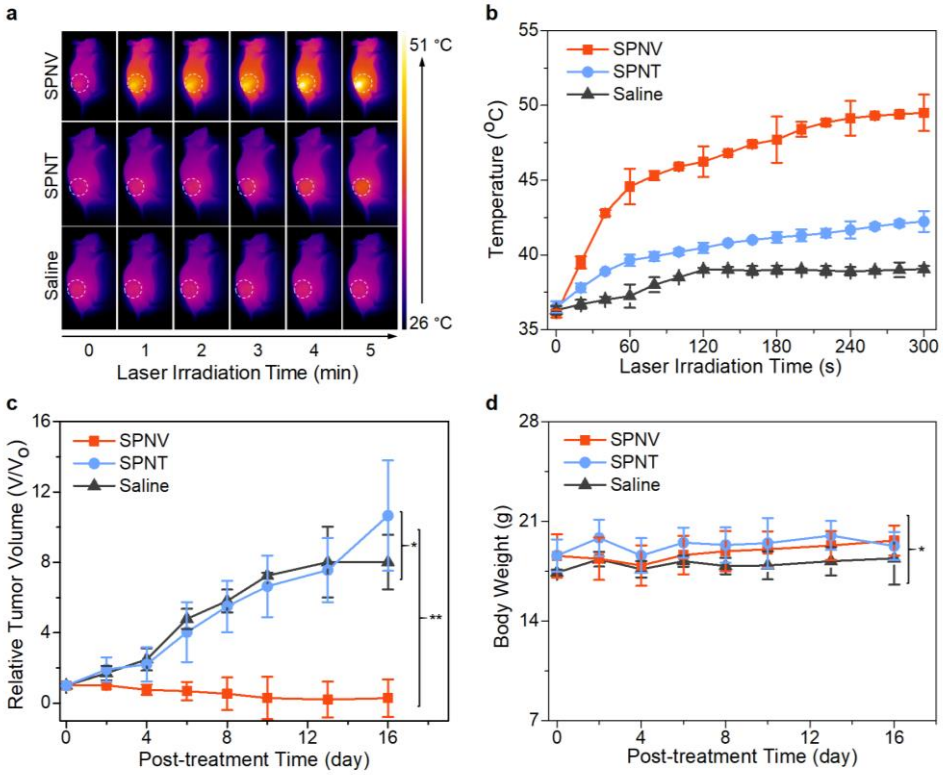

Figure 5. *In vivo* photothermal therapy of tumor. (**a**) IR thermal images of 4T1 tumor-bearing mice under laser irradiation at 808 nm with the power of 0.3 W cm^{-2} after systemic administration of saline, SPNV, or SPNT (6 mg kg^{-1} body weight) at the post-injection time of 6 h. The tumors are indicated with the white dashed circles. (**b**) Mean tumor temperature as a function of laser irradiation time after systemic administration of saline, SPNV or SPNT at the post-injection time of 6 h. (**c**) Tumor growth curves of mice after systemic treatment with saline, SPNV or SPNT with laser irradiation. (**d**) Body weight data of mice after systemic treatment with saline, SPNV or SPNT with laser irradiation. Error bars were based on the standard deviations (SD) of three parallel samples (*$p > 0.05$, **$p < 0.005$).

To evaluate the antitumor effect, the tumor volumes of SPNV- or SPNT-treated mice were continuously monitored for 16 days after laser irradiation. The tumors of SPNT-treated mice grew as fast as that of saline-treated mice (Figure 5c), which was caused by the fact that the tumor temperature was below the threshold temperature (43 °C) to

induce cell apoptosis. In contrast, the tumor growth for SPNV-treated mice was effectively inhibited during the whole tested period, indicating the effective *in vivo* ablation of cancer cells. The body weights for all groups of mice were measured at the same time and no obvious weight loss was observed, suggesting the low toxicity of all SPN treatments (Figure 5d).

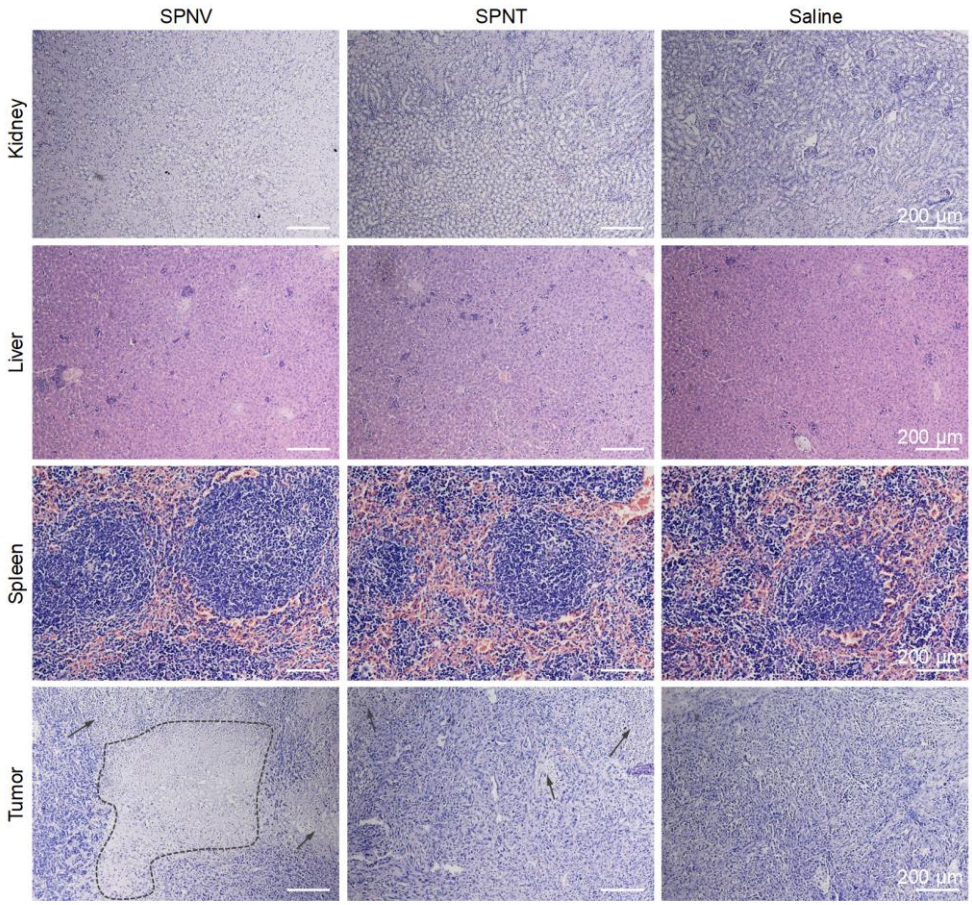

Figure 6. Histological H&E staining for kidney, liver, spleen and tumors at day 16 after the photothermal treatment with saline, SPNV or SPNT. The tumor regions with necrosis are indicated with the dashed circles and arrows.

To further verify the enhanced therapeutic outcome of SPNV, all the mice treated with SPNs or saline were sacrificed and different organs and tumors were collected for histological analysis using hematoxylin and eosin (H&E) staining. No significant

histopathological abnormalities or lesions were observed for kidney, liver and spleen of all the groups (Figure 6). In contrast, different extent of necrosis was observed for the tumor tissues of SPN-treated mice followed by PTT treatment. Large areas of necrosis were found on the tumor slides for SPNV-treated mice, which were not that obvious for SPNT-treated mice. The percentage of neurosis area on the tumor slide for SPNV-treated mice was calculated to be 54%, 9-times higher than that for SPNT-treated mice (6%). The histological analysis again proved the superior PTT outcome of SPNV over SPNT, which was consistent with the *in vivo* antitumor data.

CONCLUSIONS

We have developed an organic nanoagent (SPNV) with good biodegradability and enhanced PA and PTT efficacies relative to its counterpart. Our design took advantage of the oxidizable nature of vinylene bonds to endow SPNV with the ability to be efficiently digested in the presence of peroxidase meanwhile without comprising the optical and photothermal properties. In fact, because of the low molecular weight and planar conformation of vinylene bonds, SPNV showed mass absorption coefficient, and photothermal conversion efficacy (71%) that are respectively 1.3- and 2.4-fold higher than its counterpart nanoparticle without vinylene bonds (SPNT). It should be emphasized that the photothermal conversion efficacy of SPNV was also significantly higher than most reported photothermal agents. Thus, SPNV acted as a much better PA/PTT theranostic nanoagents than SPNT, providing amplified PA signals and maximum photothermal temperature in living mouse. Moreover, both *in vivo* tumor

growth data and *ex vivo* histological data validated the superior antitumor efficacy of SPNV over SPNT. By virtue of its good biodegradability and organically benign composition, SPNV should hold great promise for translational medicine.

In summary, our study provides a molecular design approach to enhance the biodegradability of optically-active polymer nanoparticles meanwhile dramatically elevating their photothermal capability. Such a design can be generalized for other SPs with different structures and applied for other imaging and therapy applications such as NIR fluorescence imaging guided photodynamic therapy.

METHODS

Chemicals. 3,6-Bis(5-bromothiophen-2-yl)-2,5-bis(2-hexyldecyl)pyrrolo[3,4-*c*]pyrrole-1,4(2*H*,5*H*)-dione was purchased from Luminescence Technology Corp. All chemicals were purchased from Sigma-Aldrich unless otherwise declared.

Materials Characterization. TEM images were obtained on a JEM 1400 transmission electron microscope with an accelerating voltage from 40 to 120 kV. DLS and zeta potential were carried out on the Malvern Nano-ZS Particle Size. Ultraviolet (UV)-Vis spectra were conducted on a Shimadzu UV-2450 spectrophotometer. Infrared (IR) thermal images were captured by the photothermal camera F30W from Nippon Avionics Co., Ltd.. An 808 nm high power NIR Lasers (operating mode: CW, output power after fiber: 2.5 W, LED display: diode current, multimode fiber, fiber core diameter: 400 μm, fiber connector: SMA905, with tunable laser driver module: 0−100%) purchased from CNI Co. Ltd. was used for photothermal measurements of

SPN solutions and PTT *in vivo*. The laser spot size was 1 cm^2. Nuclear Magnetic Resonance (NMR) spectroscopy was recorded on a BRUKER Avance 300 NMR (^1H: 300MHz) system with $CDCl_3$ as the solvent. The spectra were internally referenced to the tetramethylsilane signal at 0 ppm.

Synthesis of DPPV. 3,6-Bis(5-bromothiophen-2-yl)-2,5-bis(2-hexyldecyl)pyrrolo[3,4-*c*]pyrrole-1,4(2*H*,5*H*)-dione (75 mg, 0.083 mmol), trans-1,2-bis(tributylstannyl)ethene (50 mg, 0.083 mmol), $Pd_2(dba)_3$ (0.6 mg, 0.00065 mmol), and tri(*o*-tolyl)phosphine (1.2 mg, 0.0039 mmol) were placed in a Schlenk tube (50 mL). The Schlenk tube was then sealed, degassed and refilled with nitrogen by three vacuum-nitrogen cycles. Chlorotoluene (3 mL) was then injected into the tube. The mixture was degassed by three freeze-pump-thaw circles. The Stille polycondensation reaction was subsequently conducted at 100 °C by vigorous stirring under N_2 atmosphere for 24 h. The resulted dark viscous mixture was precipitated and washed three times by excess methanol. The residue was collected by centrifugation and then dried under vacuum to obtain the final product. ^1H NMR (300 MHz, $CDCl_3$, δ): 9.29 – 8.64 (m, 4H), 6.83 – 6.59 (m, 2H), 4.30-3.85 (m, 4H), 2.72-2.47 (m, 2H), 1.46-1.08 (m, 41H), 0.90-0.73 (m, 19H).

Preparation of SPNs. DPPV, DPPT and PLGA-PEG (Mn=4500) were dissolved in THF to prepare stock solutions individually. Then the THF solution (1 mL) containing DPPV or DPPT (0.25 mg) and PLGA-PEG (10 mg) were mixed and rapidly injected into the homogeneous mixture of distilled-deionized water and THF (11 mL) at the ratio of 10:1 under sonication. After sonication for additional 10 min, THF was evaporated

under nitrogen atmosphere. The aqueous solution was filtered through a polyethersulfone (PES) syringe driven filter (0.22 μm) (Millipore) and washed three times using distilled-deionized water and centrifugal filter units (Millipore, MWCO 50 kDa) with the speed of 3,500 rpm for 15 min. The SPN solutions were diluted in 1× PBS buffer (pH 7.4) and the concentrations were determined by UV-Vis absorption according to the mass absorption coefficient. The SPN solutions were finally concentrated by ultrafiltration and stored in dark at 4 °C.

***In vitro* PA Instrumentation.** *In vitro* PA spectra were measured by an optical parametric oscillator, OPO (Continuum, Surelite), generating pulses with duration 5 ns and pulse energy 100 mJ $pulse^{-1}$ at 10 Hz repetition rate, which was pumped by a Q-switched 532 nm Nd:YAG laser. The output wavelength was tuned from 680 to 900 nm. The SPNV or SPNT solution was placed inside a low-density polyethylene (LDPE) tube with an inner diameter (ID) of 0.59 mm and outer diameter (OD) of 0.78 mm. After irradiation with laser wavelengths ranging from 680 to 900 nm with 10 nm increment, the PA signals produced in LDPE tube was coupled to the single-element ultrasound transducer, UST (V323-SU 2.25 MHz^{-1}, 13 mm active area, and 70% nominal bandwidth, Panametrics). Both the tube and UST were immersed in aqueous medium. PA signals at individual wavelength were acquired using the UST, which were subsequently amplified with a gain of 50 dB. Band pass was filtered (1-10 MHz) by a pulser/receiver unit (Olympus-NDT, 5072PR) and the output was digitized with a data acquisition card (GaGe, compuscope 4227) operated at 25 MHz. Peak-to-peak voltages of the PA signals for each wavelength were then normalized relative to the laser power.

The normalized signals were plotted as a function of wavelengths to generate the PA spectra. The PA signals with different concentrations of SPNs were measured in the same way at the laser wavelength of 810 nm.

***In vitro* Biodegradability Studies.** SPNV or SPNT solutions (3 μg mL^{-1}) were incubated with H_2O_2 (300 μM) in the present or absent of MPO (50 μg mL^{-1}) at 37 °C in phosphate buffer (50 mM, pH 7.0) with NaCl (150 mM). The absorption spectra of SPNs were measured after the incubation for 0, 24 and 48 h until the peak of SPNV at 819 nm disappeared. The MPO enzyme was purchased from Bio-Techne China Co. Ltd. with specific activity >50,000 pmol min^{-1} μg^{-1}. The average MPO concentration in neutrophils was reported to be 5.9×10^{-7} U per neutrophil.[60] There are around 3000-7000 neutrophils μL^{-1} in blood. The specific activity of MPO enzyme we used is 5×10^{-2} U μg^{-1}. Subsequently the average MPO concentration can be translated to be 35.4-82.6 μg mL^{-1}.

***In vitro* Photothermal Characterizations.** The 1 × PBS solution (pH 7.4) of SPNV or SPNT with the concentration of 60 μg mL^{-1} and the same amount of PBS buffer were exposed to laser irradiation at 808 nm. The temperatures were recorded every 20 s and the laser was turned off until the temperature reaching plateau (8 minutes here). Then the temperatures were continuously monitored every 20 s for another 8 min. The heating and cooling process were repeated five times to test the photothermal stability of SPNV or SPNT. The photothermal conversion efficiencies were calculated according to our previous report.[54]

Cell Culture. 4T1 and RAW264.7 cells were purchased from the American Type

Culture Collection (ATCC). 4T1 cells were cultured in RPMI-1640 medium supplemented with fetal bovine serum (FBS, 10%) and Penicillin/Streptomycin antibiotics (1%). RAW264.7 cells were cultured in Dulbecco's Modified Eagle Medium (DMEM) supplemented with fetal bovine serum (FBS, 10%) and Penicillin/Streptomycin antibiotics (1%). The cells were maintained in an atmosphere of 5% CO2 and 95% humidified air at 37°C.

Biodegradability Studies in cells. The RAW264.7 Cells were subculture in flask. When the cell confluency reached 60%, the cells were incubated with SPNV (38 μg mL^{-1}) for 24 hours. Then the cells were washed with PBS buffer (10 mM, pH 7.4) and treated with lipopolysaccharides (LPS, 1 μg mL^{-1}) for 30 hours. The cells without LPS-treatment were served as the control group. Then the cells were harvested, counted the number and broken by ultrasonication. After centrifugation with 4, 000 rpm for 10 min, the solutions from 276, 000 cells in 1 mL PBS buffer were used to measure the absorption.

Cytotoxicity Test. Cells were seeded in 96 well plates (3000 cells in 100 μL medium per well) for 12 h, and then were cultured with fresh medium containing SPNV or SPNT solutions with different concentrations of 10, 20, 60, 100 and 150 μg mL^{-1} for 24 h. Next, the per well medium was changed to the mixture of 120 μL fresh medium with MTS solution (Promega) (20 μL). After incubation for another 4 h, the absorbance measurement at 490 nm was performed using a SpectraMax M5 microplate/cuvette reader. Cell viability was expressed as the ratio of the absorbance of the cells treated with SPNV or SPNT to that of untreated cells.

***In vitro* PTT of SPNs.** Cells were seeded in 96 well plates (10, 000 cells in 100 μL medium per well) for 12 h, and followed by incubation with fresh medium containing SPNV or SPNT solutions with different concentrations of 20, 60 and 100 μg mL^{-1} for 3 h. After it, the cells were irradiated with 808 nm laser with different power densities of 0.3 and 0.5 W cm^{-2} for 8 min and followed by incubation with fresh medium for another 12 h. At last, the cell viabilities were measured and calculated as described in the Cytotoxicity Test section.

Tumor Mouse Model. All animal studies were performed under protocols approved by Laboratory Animal Center of Soochow University. To establish tumors in eight-week-old BALB/c, ten to twenty million 4T1 cells were suspended in 1 mL fresh medium and each mouse was subcutaneously injected with 0.1 mL cell suspension under the armpit. Tumors were allowed to grow to a single aspect ~7 mm (approximately 10–15 days) before *in vivo* experiments.

***In Vivo* PA Imaging.** After mice bearing 4T1 tumors were anesthetized using 2% isoflurane in oxygen, SPNV or SPNT solutions were systematically injected through the tail vein using a microsyringe (6 mg kg^{-1} body weight) (n=3). A Multispectral Optoacoustic Tomography scanner (MSOT, iThera medical, Germany) was used to acquire the PA images at 810 nm. *In vivo* PA spectra with excitation light from 680 to 850 nm were acquired from the tumor regions after 6 h systemic administration of SPNs.

***In Vivo* PTT.** Mice bearing 4T1 tumors were exposed to 808 nm laser with the power density of 0.3 W cm^{-2} after systemic administration of saline (200 μL) (n=3), SPNV (6

mg kg^{-1} body weight) (n=3) or SPNT (6 mg kg^{-1} body weight) (n=3) for 6 h. IR thermal camera was utilized to record the temperature change of the tumor in every 20 seconds during the laser irradiation of 5 min. The tumor sizes were measured by caliper every other day and calculated as the volume = (tumor length) × (tumor width)^2/2. Relative tumor sizes were calculated as V/V_o (V_o was the initial tumor volume).

Biodistribution Method. After 24 h post-injection of SPNV or SPNT, the mice were sacrificed by CO_2 asphyxiation. Major organs as indicated were harvested for the PA measurements.

Histological Studies. The mice treated with saline (200 μl) (n=3), SPNV (6 mg kg^{-1} body weight) (n=3) or SPNT (6 mg kg^{-1} body weight) (n=3) and followed by PTT treatment were sacrificed. The kidney, liver, spleen and tumor were fixed in 4% formalin and then conducted with paraffin-embedded section for H&E staining. The slices were examined by a digital microscope (Leica).

Data Analysis. *In vivo* and *ex vivo* PA intensities were measured by region of interest (ROI) analysis using post-processing software ViewMSOT. The histological analysis was carried out using Image J. Results were expressed as the mean± standard deviations (SD) unless otherwise stated.

ASSOCIATED CONTENTS

The authors declare no competing financial interest.

Supporting Information

The Supporting Information is available free of charge on the ACS Publications website.

The stability, *in vitro* cytotoxicity study and *ex vivo* biodistribution of SPNs (PDF).

AUTHOR INFORMATION

Corresponding Author

*Email: xinlou301@sina.com.

*Email: kypu@ntu.edu.sg

ORCID

Mingyuan Gao: 0000-0002-7360-3684

Kanyi Pu: 0000-0002-8064-6009

Author Contributions

The manuscript was written through contributions of all authors. All authors have given approval to the final version of the manuscript. Y. Lyu and J. Zeng contributed equally.

ACKNOWLEDGMENT

K.P. thanks Nanyang Technological University (Start-Up grant: NTU-SUG: M4081627.120) and Singapore Ministry of Education (Academic Research Fund Tier 1: RG133/15 M4011559, 2017-T1-002-134-RG147/17, and Tier 2 MOE2016-T2-1-098) for the financial support. M.G. thanks the National Natural Science Foundation of China (81530057).

REFERENCES

1. Ng, K. K.; Zheng, G. Molecular Interactions in Organic Nanoparticles for Phototheranostic Applications. *Chem. Rev.* **2015,** *115*, 11012-11042.
2. Fan, W.; Shen, B.; Bu, W.; Chen, F.; Zhao, K.; Zhang, S.; Zhou, L.; Peng, W.; Xiao, Q.; Xing, H.; Liu, J.; Ni, D.; He, Q.; Shi, J. Rattle-Structured Multifunctional Nanotheranostics for Synergetic Chemo-/Radiotherapy and Simultaneous Magnetic/Luminescent Dual-Mode Imaging. *J. Am. Chem. Soc.* **2013,** *135*, 6494-6503.
3. Jokerst, J. V.; Gambhir, S. S. Molecular Imaging with Theranostic Nanoparticles. *Acc. Chem. Res.* **2011,** *44*, 1050-1060.
4. Yang, K.; Feng, L.; Shi, X.; Liu, Z. Nano-Graphene in Biomedicine: Theranostic Applications. *Chem. Soc. Rev.* **2013,** *42*, 530-547.
5. Qin, C.; Liu, H.; Chen, K.; Hu, X.; Ma, X.; Lan, X.; Zhang, Y.; Cheng, Z. Theranostics of Malignant Melanoma with $^{64}CuCl_2$. *J. Nucl. Med.* **2014,** *55*, 812-817.
6. Ma, X.; Cheng, K.; Cutler, C.; Bu, L.; Sun, Y.; Kang, F.; Yang, W.; Wang, J.; Cheng, Z. Cerenkov Luminescence Transfer Based Gold-198 Nanocluster for Tumor *in vivo* Imaging and Therapy. *J. Nucl. Med.* **2015,** *56*, 61.
7. Jiang, X.; Zhang, S.; Ren, F.; Chen, L.; Zeng, J.; Zhu, M.; Cheng, Z.; Gao, M.; Li, Z. Ultrasmall Magnetic $CuFeSe_2$ Ternary Nanocrystals for Multimodal Imaging Guided Photothermal Therapy of Cancer. *ACS Nano* **2017,** *11*, 5633-5645.
8. Min, K.; Min, H.; Lee, H.; Park, D.; Yhee, J.; Kim, K.; Kwon, I. C.; Jeong, S. Y.; Silvestre, O. F.; Chen, X.; Hwang, Y. S.; Kim, E. C.; Lee, S. C. pH-Controlled Gas-Generating Mineralized Nanoparticles: A Theranostic Agent for Ultrasound Imaging and Therapy of Cancers. *ACS Nano* **2015,** *9*, 134-145.
9. Ke, H.; Wang, J.; Dai, Z.; Jin, Y.; Qu, E.; Xing, Z.; Guo, C.; Yue, X.; Liu, J. Gold-Nanoshelled Microcapsules: A Theranostic Agent for Ultrasound Contrast Imaging and Photothermal Therapy. *Angew. Chem., Int. Ed.* **2011,** *50*, 3017-3021.
10. Melancon, M. P.; Zhou, M.; Li, C. Cancer Theranostics with Near-Infrared Light-Activatable Multimodal Nanoparticles. *Acc. Chem. Res.* **2011,** *44*, 947-956.
11. Gong, H.; Dong, Z.; Liu, Y.; Yin, S.; Cheng, L.; Xi, W. Y.; Xiang, J.; Liu, K.; Li, Y.; Liu, Z. Engineering of Multifunctional Nano-Micelles for Combined Photothermal and Photodynamic Therapy Under the Guidance of Multimodal Imaging. *Adv. Funct. Mater.* **2014,** *24*, 6492-6502.
12. Song, J.; Yang, X.; Yang, Z.; Lin, L.; Liu, Y.; Zhou, Z.; Shen, Z.; Yu, G.; Dai, Y.; Jacobson, O.; Munasinghe, J.; Yung, B.; Teng, G.; Chen, X. Rational Design of Branched Nanoporous Gold Nanoshells with Enhanced Physico-Optical Properties for Optical Imaging and Cancer Therapy. *ACS Nano* **2017,** *11*, 6102-6113.
13. Chen, Q.; Xu, L. G.; Liang, C.; Wang, C.; Peng, R.; Liu, Z. Photothermal Therapy with Immune-Adjuvant Nanoparticles Together with Checkpoint Blockade for Effective Cancer Immunotherapy. *Nat. Commun.* **2016,** *7*, 13193.
14. Wang, L. V.; Hu, S. Photoacoustic Tomography: *In Vivo* Imaging from Organelles to Organs. *Science* **2012,** *335*, 1458-1462.
15. Zhang, H.; Maslov, K.; Stoica, G.; Wang, L. V. Functional Photoacoustic Microscopy for High-Resolution and Noninvasive *in Vivo* Imaging. *Nat. Biotechnol.* **2006,** *24*, 848-851.
16. Wang, L. V. Multiscale Photoacoustic Microscopy and Computed Tomography. *Nat.*

Photonics **2009,** *3*, 503-509.
17. Razansky, D.; Deliolanis, N. C.; Vinegoni, C.; Ntziachristos, V. Deep Tissue Optical and Optoacoustic Molecular Imaging Technologies for Pre-Clinical Research and Drug Discovery. *Curr. Pharm. Biotechnol.* **2012,** *13*, 504-522.
18. Yu, J.; Yang, C.; Li, J.; Ding, Y.; Zhang, L.; Yousaf, M.; Lin, J.; Pang, R.; Wei, L.; Xu, L.; Sheng, F.; Li, C.; Li, G.; Zhao, L.; Hou, Y. Multifunctional Fe_5C_2 Nanoparticles: A Targeted Theranostic Platform for Magnetic Resonance Imaging and Photoacoustic Tomography-Guided Photothermal Therapy. *Adv. Mater.* **2014,** *26*, 4114-4120.
19. Lyu, Y.; Fang, Y.; Miao, Q.; Zhen, X.; Ding, D.; Pu, K. Intraparticle Molecular Orbital Engineering of Semiconducting Polymer Nanoparticles as Amplified Theranostics for *in Vivo* Photoacoustic Imaging and Photothermal Therapy. *ACS Nano* **2016,** *10*, 4472-4481.
20. Zhu, H.; Lai, Z.; Fang, Y.; Zhen, X.; Tan, C.; Qi, X.; Ding, D.; Chen, P.; Zhang, H.; Pu, K. Ternary Chalcogenide Nanosheets with Ultrahigh Photothermal Conversion Efficiency for Photoacoustic Theranostics. *Small* **2017,** *13*, 1604139.
21. Jiang, Y.; Cui, D.; Fang, Y.; Zhen, X.; Upputuri, P. K.; Pramanik, M.; Ding, D.; Pu, K. Amphiphilic Semiconducting Polymer as Multifunctional Nanocarrier for Fluorescence/Photoacoustic Imaging Guided Chemo-Photothermal Therapy. *Biomaterials* **2017,** *145*, 168-177.
22. Levi, J.; Kothapalli, S. R.; Ma, T.; Hartman, K.; Khuri-Yakub, B. T.; Gambhir, S. S. Design, Synthesis, and Imaging of an Activatable Photoacoustic Probe. *J. Am. Chem. Soc.* **2010,** *132*, 11264-11269.
23. Zhang, Y.; Cai, X.; Wang, Y.; Zhang, C.; Li, L.; Choi, S. W.; Wang, L. V.; Xia, Y. Noninvasive Photoacoustic Microscopy of Living Cells in Two and Three Dimensions through Enhancement by a Metabolite Dye. *Angew. Chem., Int. Ed.* **2011,** *50*, 7359-7363.
24. Lovell, J. F.; Jin, C.; Huynh, E.; Jin, H.; Kim, C.; Rubinstein, J. L.; Chan, W. C. W.; Cao, W.; Wang, L.; Zheng, G. Porphysome Nanovesicles Generated by Porphyrin Bilayers for Use as Multimodal Biophotonic Contrast Agents. *Nat. Mater.* **2011,** *10*, 324-332.
25. Huynh, E.; Lovell, J. F.; Helfield, B. L.; Jeon, M.; Kim, C.; Goertz, D. E.; Wilson, B. C.; Zheng, G. Porphyrin Shell Microbubbles with Intrinsic Ultrasound and Photoacoustic Properties. *J. Am. Chem. Soc.* **2012,** *134*, 16464-16467.
26. Abbas, M.; Zou, Q.; Li, S.; Yan, X. Self-Assembled Peptide- and Protein-Based Nanomaterials for Antitumor Photodynamic and Photothermal Therapy. *Adv. Mater.* **2017,** *29,* 1605021.
27. Liu, K.; Xing, R.; Zou, Q.; Ma, G.; Mohwald, H.; Yan, X. Simple Peptide-Tuned Self-Assembly of Photosensitizers towards Anticancer Photodynamic Therapy. *Angew. Chem., Int. Ed.* **2016,** *55*, 3036-3039.
28. Xing, R.; Liu, K.; Jiao, T.; Zhang, N.; Ma, K.; Zhang, R.; Zou, Q.; Ma, G.; Yan, X. An Injectable Self-Assembling Collagen-Gold Hybrid Hydrogel for Combinatorial Antitumor Photothermal/Photodynamic Therapy. *Adv. Mater.* **2016,** *28*, 3669-3676.
29. Zou, Q.; Abbas, M.; Zhao, L.; Li, S.; Shen, G.; Yan, X. Biological Photothermal Nanodots Based on Self-Assembly of Peptide-Porphyrin Conjugates for Antitumor

Therapy. *J. Am. Chem. Soc.* **2017,** *139*, 1921-1927.
30. Ku, G.; Zhou, M.; Song, S.; Huang, Q.; Hazle, J.; Li, C. Copper Sulfide Nanoparticles As a New Class of Photoacoustic Contrast Agent for Deep Tissue Imaging at 1064 nm. *ACS Nano* **2012,** *6*, 7489-7496.
31. Kim, J. W.; Galanzha, E. I.; Shashkov, E. V.; Moon, H. M.; Zharov, V. P. Golden Carbon Nanotubes as Multimodal Photoacoustic and Photothermal High-Contrast Molecular Agents. *Nat. Nanotechnol.* **2009,** *4*, 688-694.
32. Murakami, T.; Nakatsuji, H.; Inada, M.; Matoba, Y.; Umeyama, T.; Tsujimoto, M.; Isoda, S.; Hashida, M.; Imahori, H. Photodynamic and Photothermal Effects of Semiconducting and Metallic-Enriched Single-Walled Carbon Nanotubes. *J. Am. Chem. Soc.* **2012,** *134*, 17862-17865.
33. De La Zerda, A.; Zavaleta, C.; Keren, S.; Vaithilingam, S.; Bodapati, S.; Liu, Z.; Levi, J.; Smith, B. R.; Ma, T.; Oralkan, O.; Cheng, Z.; Chen, X.; Dai, H.; Khuri-Yakub, B. T.; Gambhir, S. S. Carbon Nanotubes as Photoacoustic Molecular Imaging Agents in Living Mice. *Nat. Nanotechnol.* **2008,** *3*, 557-562.
34. Patel, M. A.; Yang, H.; Chiu, P. L.; Mastrogiovanni, D. D. T.; Flach, C. R.; Savaram, K.; Gomez, L.; Hemnarine, A.; Mendelsohn, R.; Garfunkel, E.; Jiang, H.; He, H. Direct Production of Graphene Nanosheets for Near Infrared Photoacoustic Imaging. *ACS Nano* **2013,** *7*, 8147-8157.
35. Sharifi, S.; Behzadi, S.; Laurent, S.; Forrest, M. L.; Stroeve, P.; Mahmoudi, M. Toxicity of Nanomaterials. *Chem. Soc. Rev.* **2012,** *41*, 2323-2343.
36. Liu, J.; Wang, P.; Zhang, X.; Wang, L.; Wang, D.; Gu, Z.; Tang, J.; Guo, M.; Cao, M.; Zhou, H.; Liu, Y.; Chen, C. Rapid Degradation and High Renal Clearance of Cu_3BiS_3 Nanodots for Efficient Cancer Diagnosis and Photothermal Therapy *in Vivo*. *ACS Nano* **2016,** *10*, 4587-4598.
37. Zhang, J.; Zhang, J.; Li, W.; Chen, R.; Zhang, Z.; Zhang, W.; Tang, Y.; Chen, X.; Liu, G.; Lee, C. Degradable Hollow Mesoporous Silicon/Carbon Nanoparticles for Photoacoustic Imaging-Guided Highly Effective Chemo-Thermal Tumor Therapy *in Vitro* and *in Vivo*. *Theranostics* **2017,** *7*, 3007-3020.
38. Song, G.; Hao, J.; Liang, C.; Liu, T.; Gao, M.; Cheng, L.; Hu, J.; Liu, Z. Degradable Molybdenum Oxide Nanosheets with Rapid Clearance and Efficient Tumor Homing Capabilities as a Therapeutic Nanoplatform. *Angew. Chem., Int. Ed.* **2016,** *55*, 2122-2126.
39. Chen, Y.; Cheng, L.; Dong, Z.; Chao, Y.; Lei, H.; Zhao, H.; Wang, J.; Liu, Z. Degradable Vanadium Disulfide Nanostructures with Unique Optical and Magnetic Functions for Cancer Theranostics. *Angew. Chem., Int. Ed.* **2017,** *56*, 12991-12996.
40. Lyu, Y.; Pu, K. Recent Advances of Activatable Molecular Probes Based on Semiconducting Polymer Nanoparticles in Sensing and Imaging. *Adv. Sci.* **2017,** *4*, 1600481.
41. Xu, L.; Cheng, L.; Wang, C.; Peng, R.; Liu, Z. Conjugated Polymers for Photothermal Therapy of Cancer. *Polym. Chem.* **2014,** *5*, 1573-1580.
42. Zhu, C. L.; Liu, L. B.; Yang, Q.; Lv, F. T.; Wang, S. Water-Soluble Conjugated Polymers for Imaging, Diagnosis, and Therapy. *Chem. Rev.* **2012,** *112*, 4687-4735.
43. Wu, C.; Chiu, D. T. Highly Fluorescent Semiconducting Polymer Dots for Biology

and Medicine. *Angew. Chem., Int. Ed.* **2013,** *52*, 3086-3109.
44. Pu, K.; Chattopadhyay, N.; Rao, J. Recent Advances of Semiconducting Polymer Nanoparticles in *in Vivo* Molecular Imaging. *J. Controlled Release* **2016,** *240*, 312-322.
45. Yin, C.; Zhen, X.; Zhao, H.; Tang, Y.; Ji, Y.; Lyu, Y.; Fan, Q.; Huang, W.; Pu, K. Amphiphilic Semiconducting Oligomer for Near-Infrared Photoacoustic and Fluorescence Imaging. *ACS Appl. Mater. Interfaces* **2017,** *9*, 12332-12339.
46. Zhu, H.; Fang, Y.; Zhen, X.; Wei, N.; Gao, Y.; Luo, K.; Xu, C. J.; Duan, H.; Ding, D.; Chen, P.; Pu, K. Multilayered Semiconducting Polymer Nanoparticles with Enhanced NIR Fluorescence for Molecular Imaging in Cells, Zebrafish and Mice. *Chem. Sci.* **2016,** *7*, 5118-5125.
47. Zhen, X.; Zhang, C.; Xie, C.; Miao, Q.; Lim, K.; Pu, K. Intraparticle Energy Level Alignment of Semiconducting Polymer Nanoparticles to Amplify Chemiluminescence for Ultrasensitive *In Vivo* Imaging of Reactive Oxygen Species. *ACS Nano* **2016,** *10*, 6400-6409.
48. Shuhendler, A. J.; Pu, K.; Cui, L.; Uetrecht, J. P.; Rao, J. H. Real-Time Imaging of Oxidative and Nitrosative Stress in the Liver of Live Animals for Drug-Toxicity Testing. *Nat. Biotechnol.* **2014,** *32*, 373-380.
49. Pu, K.; Shuhendler, A. J.; Jokerst, J. V.; Mei, J.; Gambhir, S. S.; Bao, Z.; Rao, J. Semiconducting Polymer Nanoparticles as Photoacoustic Molecular Imaging Probes in Living Mice. *Nat. Nanotechnol.* **2014,** *9*, 233-239.
50. Pu, K.; Mei, J.; Jokerst, J. V.; Hong, G.; Antaris, A. L.; Chattopadhyay, N.; Shuhendler, A. J.; Kurosawa, T.; Zhou, Y.; Gambhir, S. S.; Bao, Z.; Rao, J. Diketopyrrolopyrrole-Based Semiconducting Polymer Nanoparticles for *In Vivo* Photoacoustic Imaging. *Adv. Mater.* **2015,** *27*, 5184-5190.
51. Miao, Q.; Xie, C.; Zhen, X.; Lyu, Y.; Duan, H.; Liu, X.; Jokerst, J. V.; Pu, K. Molecular Afterglow Imaging with Bright, Biodegradable Polymer Nanoparticles. *Nat. Biotechnol.* **2017,** *35*, 1102-1110.
52. Zhu, H.; Fang, Y.; Miao, Q.; Qi, X.; Ding, D.; Chen, P.; Pu, K. Regulating Near-Infrared Photodynamic Properties of Semiconducting Polymer Nanotheranostics for Optimized Cancer Therapy. *ACS Nano* **2017,** *11*, 8998-9009.
53. Lyu, Y.; Cui, D.; Sun, H.; Miao, Y.; Duan, H.; Pu, K. Dendronized Semiconducting Polymer as Photothermal Nanocarrier for Remote Activation of Gene Expression. *Angew. Chem., Int. Ed.* **2017,** *56*, 9155-9159.
54. Lyu, Y.; Xie, C.; Chechetka, S. A.; Miyako, E.; Pu, K. Semiconducting Polymer Nanobioconjugates for Targeted Photothermal Activation of Neurons. *J. Am. Chem. Soc.* **2016,** *138*, 9049-9052.
55. Xie, C.; Upputuri, P. K.; Zhen, X.; Pramanik, M.; Pu, K. Self-Quenched Semiconducting Polymer Nanoparticles for Amplified *in Vivo* Photoacoustic Imaging. *Biomaterials* **2017,** *119*, 1-8.
56. Mecking, S. Nature or Petrochemistry? Biologically Degradable Materials. *Angew. Chem., Int. Ed.* **2004,** *43*, 1078-1085.
57. Shao, J.; Xie, H.; Huang, H.; Li, Z.; Sun, Z.; Xu, Y.; Xiao, Q.; Yu, X.; Zhao, Y.; Zhang, H.; Wang, H.; Chu, P. Biodegradable Black Phosphorus-Based Nanospheres for *in Vivo* Photothermal Cancer Therapy. *Nat. Commun.* **2016,** *7*, 12967.

58. Vezie, M. S.; Few, S.; Meager, I.; Pieridou, G.; Dorling, B.; Ashraf, R. S.; Goni, A. R.; Bronstein, H.; McCulloch, I.; Hayes, S. C.; Campoy-Quiles, M.; Nelson, J. Exploring the Origin of High Optical Absorption in Conjugated Polymers. *Nat. Mater.* **2016,** *15*, 746-753.
59. Schwartz, B. J. Conjugated Polymers as Molecular Materials : How Chain Conformation and Film Morphology Influence Energy Transfer and Interchain Interactions. *Annu. Rev. Phys. Chem.* **2003,** *54*, 141-172.
60. Christensen, R. D.; Rothstein, G. Neutrophil Myeloperoxidase Concentration - Changes with Development and during Bacterial-Infection. *Pediatr. Res.* **1985,** *19*, 1278-1282.
61. Klebanoff, S. J. Myeloperoxidase: Friend and Foe. *J. Leukocyte Biol.* **2005,** *77*, 598-625.
62. Gomez-Mejiba, S. E.; Zhai, Z.; Gimenez, M. S.; Ashby, M. T.; Chilakapati, J.; Kitchin, K.; Mason, R. P.; Ramirez, D. C. Myeloperoxidase-induced Genomic DNA-centered Radicals. *J. Biol. Chem.* **2010,** *285,* 20062-20071.

TOC

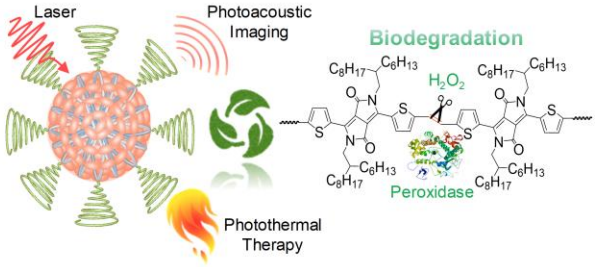
Laser
Photoacoustic Imaging
Biodegradation
H_2O_2
Peroxidase
Photothermal Therapy